Ultra compact bend-less Mach-Zehnder modulator based on GSST phase change material

SOHRAB MOHAMMADI-POUYAN,[1,*] ◉ MOHAMMADMOEIN AFROUZMEHR,[2] AND DEREK ABBOTT[3]

[1] *School of Electrical and Computer Engineering, Shiraz University, Shiraz 71348-51154, Iran*
[2] *Klipsch School of Electrical and Computer Engineering, New Mexico State University, Las Cruces NM 88011, USA*
[3] *School of Electrical and Electronic Engineering, The University of Adelaide, Adelaide, SA 5005, Australia*
[*] *s.pouyan@shirazu.ac.ir*

Abstract: Optical phase change materials (O-PCMs) are emerging as promising active materials for exploitation in silicon photonics platforms, due to their compatibility with CMOS fabrication technology and the tunability of their optical characteristics via external excitation. Despite their advantages, O-PCMs suffer from relatively high insertion loss hindering efficient modulation. Also, the change of the imaginary part of the refractive index in O-PCMs is large and the realization of a Mach-Zehnder modulator (MZM) based on O-PCM materials becomes challenging. To overcome these issues, we consider the variation of both real and imaginary parts of the refractive index, facilitated by a GSST-based MZM design. To achieve this, we design an active waveguide that is constructed via depositing an ITO layer (as the microheater) surrounding the pre-fabricated GSST layer on a silicon rib-waveguide. The active length of the proposed MZM is designed ~4.3 μm at the wavelength of 1.55 μm. The simulations indicate that a compact MZM can be achieved by eliminating the S-bends in the MZM structure without affecting the modulation. The proposed bend-less MZM demonstrates an insertion loss less than 1.7 dB and an extinction ratio greater than 35 dB over the entire optical C-band.

1. Introduction

Photonics has emerged a leading technology in recent years and this is escalating via the introduction of modern optical applications [1,2], and its compatibility with electronic fabrication technology [3]. Standard active devices based on silicon-on-insulator (SOI) platforms have a large footprint and relatively high power consumption due to a very low variation of the real part of the refractive index of the active region [4,5]. Hybrid SOI platforms based on a range of materials such as graphene [6], indium tin oxide (ITO) [2], zinc oxide [7], and zinc sulfide (ZnS) [7] have overcome the abovementioned issue. Optical phase change materials (O-PCMs) such as VO_2 [8,9], Ge-Sb-Te (GST) alloys [1,3], and $Ge_2Sb_2Se_4Te_1$ (GSST) [4,10–12], Sb_2Se_3 [13,14], and Sb_2S_3 [14,15] have become quickly attractive as an alternative option for hybrid SOI structures due to their desired characteristics [4]. Many O-PCM applications employ a reversible phase transition between opaque and transparent states via a source of actuation that can be induced, thermally [5,8,16], electrically [8,9], or optically [17]. As a result, a range of optical devices based on O-PCM materials including modulators [9,18–20], switches [4], memories [21], metasurfaces [22], Bragg gratings [23], phase shifters [13], and light manipulation devices [1] have been introduced recently. Note that O-PCM materials generally benefit from a high extinction ratio (ER), while they suffer from high insertion loss (IL) [24], and relatively low operating speed [18,24]. Among O-PCMs, GSST is chosen as a promising material due to its lower IL [25] over a broad range of wavelengths from 1 μm to 18.5 μm [10]. Here, GSST shows

a significant change in both real and imaginary parts of the refractive index and this feature is used for fabricating high-performance devices such as switches [4,11,26] and memories [21]. Mach-Zehnder modulators (MZMs) based on O-PCM have been seldom reported in the literature due to the lack of an appropriate solution to the high variations in both real and imaginary parts of the O-PCM refractive index [1,3,21]. Employing the variation of both real and imaginary parts at the same time is expected facilitate the design of a GSST-based MZM with a shorter active length and efficient modulation.

The paper is organized as follows. In section 2, a GSST/Si active waveguide is introduced to act as the arms of an MZI structure. A designed compact-modulator using a GSST-based MZM operating at the communications wavelength of 1.55 μm with the use of an ITO microheater for the excitation mechanism is simulated in section 3 that contains the calculations of the geometric parameters of the active waveguide followed with the design and characterization of the proposed GSST-MZM using an innovative approach to carry out the calculations. The electro-thermal simulations have been performed where the proper specifications including phase-transition delay, actuating signal properties, and power consumption are determined.

2.   Proposed modulator

The GSST/Si-based modulator is depicted in Fig. 1. A thin layer of GSST material is deposited on a silicon waveguide. An ITO layer is placed on the GSST region as a heater for tailoring the refractive index via the Joule heating mechanism [10,11]. The height and width of the silicon waveguide are labeled with H and W, respectively (Fig. 1(b)). Also, the thickness of the GSST layer is represented as t, and the thickness of the ITO layer is considered to be 50 nm. Here, W and H are chosen to be 480 nm and 220 nm, respectively for the waveguide to support just the transverse-electric (TE) mode at the wavelength of 1.55 μm. Two metallic contact pads are used for applying voltage to actuate the modulator. The distance between the metallic pads and the GSST region should be far enough to avoid excess optical loss.
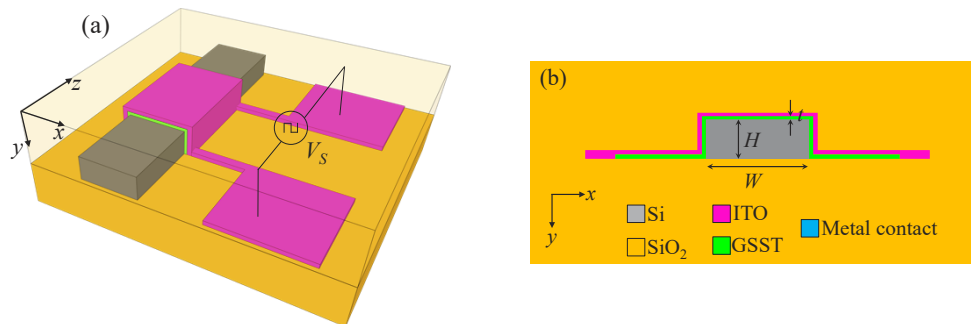

Fig. 1. (a) Bird's eye view schematic diagram of the active waveguide based on GSST/Si platform, (b) cross-section of the active waveguide with geometrical parameters.

With these dimensions, the effective refractive index of the silicon waveguide is simulated to be 2.343 at a wavelength of 1.55 μm. The refractive index of GSST will be substantially modified when the temperature of the GSST layer exceed the temperature of ~523 K which is known as the critical temperature [4]. This intense variation of refractive index in GSST is due to a phase transition in which the phase is altered from a low-loss amorphous phase to a lossy crystalline one [26]. The phase transition occurs when the current passes through the microheater by applying sufficient voltage to the ITO layer. It causes the underlying GSST to be heated up via the Joule heating mechanism. The corresponding refractive indices of the GSST in the amorphous and

crystalline phases are $3.3258 + j1.8 \times 10^{-4}$ and $5.0830 + j0.350$, respectively at the wavelength of 1.55 μm [4].

Note that transparent conducting oxides including fluorine-doped tine oxide (FTO) and ITO is the commonly reported material for fabricating microheaters for GSST-/GST-based devices [4,16,16,27,28]. However, materials such as graphene [8,9,29], doped silicon [30], and gold microheater [31] have been considered for heaters, but their fabrication suffers from relatively high complexity. Herein, ITO is considered as the material choice of the heating-device. In the simulations, the carrier concentration of ITO is considered to be 1×10^{19} cm^{-3} results in the refractive index of $1.9615 + j0.0059$ at the wavelength of 1.55 μm that is calculated by Drude-Lorentz model.

Since the refractive indices of the amorphous GSST and silicon are almost equal, and also, due to the thin-basis of the GSST layer, the optical mode is mainly confined in the silicon waveguide. This is denoted as the OFF-state of the modulator while no voltage is applied to the heater as the imaginary part of the refractive index of GSST is negligible. On the other hand, the refractive index of crystalline GSST is greater than the that of silicon. Therefore, a noticeable fraction of the optical mode is confined in the GSST layer where the large imaginary part of the refractive index of GSST causes a significant loss in the optical mode. This state is called the ON-state of the modulator established by applying sufficient voltage to the heater.

However, Mach-Zehnder interferometers (MZI) as GSST optical switches have been previously reported [4,25,26] due to the high variation of real part of the refractive index of GSST, and its low insertion loss. Here, an MZI structure has been introduced for a high-performance GSST modulator. Such modulator is expected to show low insertion loss, high extinction ratio, and a small footprint. In the next section, we find the appropriate thickness of the GSST layer to be used in the MZI structure. Next, the Mach-Zehnder modulator (MZM) will be introduced and the geometric properties will be calculated through simulation. Finally, the simulation results of the heating process of GSST will be determined in terms of power consumption and phase transition delay.

3.　Design and characterization of optical and electrical properties of the MZM

3.1.　Calculation of GSST layer thickness

The optical properties of the introduced modulator are highly dependent on the GSST active layer with a direct relation to the layer thickness (t). In order to find the appropriate value for t, it is swept from 0 to 50 nm. At each step, for the first four modes of the modulator, the real part of the effective refractive index at the wavelength of 1.55 μm in both ON- and OFF-states are simulated and the results are shown in Fig. 2. At ON-state, the modulator supports two distinct TE-polarized modes for $t > 24$ nm. In the presence of the second propagating mode, a portion of the incident light from the silicon access-waveguide will be coupled into the second TE-mode. This will degrade the performance of MZM. On the other hand, a thicker GSST layer causes a greater difference between the refractive indices of ON- and OFF-states. It results in a shorter MZM with modified functionality. Herein, t is determined to be 20 nm to fulfil both abovementioned criteria.

The effective refractive indices in ON- and OFF-states are calculated to be $2.732 + j0.0464$ and $2.551 + j2 \times 10^{-5}$, respectively at the wavelength of 1.55 μm. The amount of total coupling loss, CL, from silicon access-waveguide to the modulator and vice versa as a function of t at the wavelength of 1.55 μm is shown in Fig. 3.

Note that although the modulator supports a second mode for $t = 20$ nm, it is TM-polarized that is weakly coupled to the TE-polarized mode of the silicon access-waveguide (coupling efficiency is in the order of 10^{-13}).

By taking $t = 20$ nm, the refractive indices for the ON-state are $2.732 + j0.0464$ (TE) and $2.1391 + j0.0545$ (TM), and for that of OFF-state to be 2.551 (TE) and 1.903 (TM). The dominant
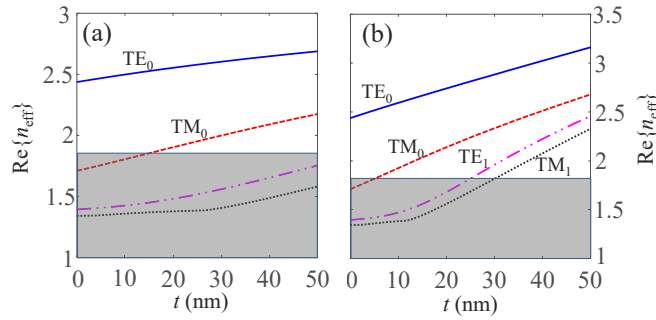
Fig. 2. The variation of real part of the effective refractive index of the modulator for the first four modes as a function of t at the wavelength of 1.55 µm in (a). OFF-state, (b). ON-state. Shaded area represents the weakly confined modes which are not considered to be propagating modes.
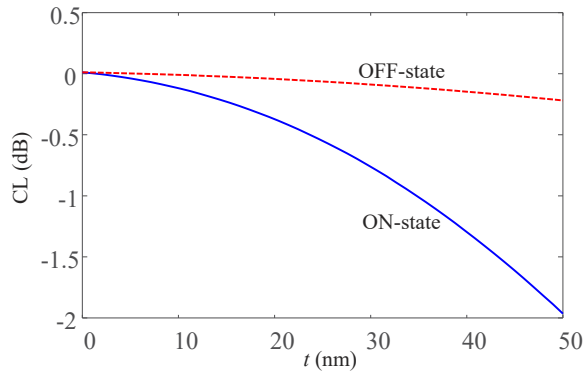

Fig. 3. The total coupling loss from silicon waveguide to the modulator as a function of t at the wavelength of 1.55 µm for the ON- and OFF-states.

components of the electric field for each mode of the modulator at the wavelength of 1.55 µm in both ON- and OFF-states are plotted in Fig. 4.
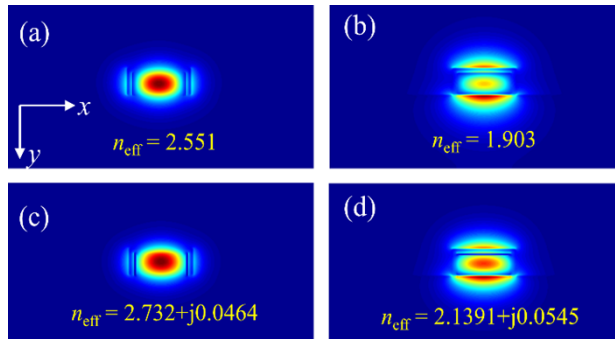

Fig. 4. The dominant components of the electric field of the modulator for the TE (E_x) and TM (E_y) modes in (a, b) the OFF-state, and (c, d) for that of ON-state.

As an electro-absorption modulator with the designed dimensions, the insertion loss (IL) and the extinction ratio (ER = IL_{OFF} − IL_{ON}) are calculated 1.4×10^{-3} dB/µm and of 2.034

dB/µm, respectively. Also, it can be considered as a phase-modulator with the efficiency of 0.733 rad/µm. To ensure realistic results, all optical simulations are performed by considering the wavelength-dependency of refractive indices of the exploited materials.

In brief, the fabrication process for the designed modulator can be described as follows. Starting with the silicon rib-waveguide on an SOI platform. For fabricating the GSST region surrounding the Si-waveguide, a standard lithography and the lift-off procedure can be performed. The GSST layer can be deposited using the atomic layer deposition (ALD) method [11,32], and a similar process would be utilized for fabricating the ITO microheater.

3.2. Propose and design of MZM

The finite loss in the crystalline phase makes it challenging for realizing a GSST-based MZM. Although, a few MZI-based O-PCM devices have been reported previously [1,3,21], but it appears these designs are not based on insightful physical and optical calculations. For example, a GSST-based device proposed in [21] exploited a neural network method to determine an appropriate amount of GSST material on a portion of MZI arm to act as the active arm. As a result, there was no insight into how the physical theories behind their design can be considered. On the other hand, it seems that the device arms are balanced by compensating the excess loss of the crystalline state by adding a lossy region on the passive arm that causes an increase in the total insertion loss. To address these issues, we have proposed a MZI structure for the active materials that the variation of real part of the refractive index comes with that of the imaginary part. The proposed MZM structure is shown in Fig. 5.
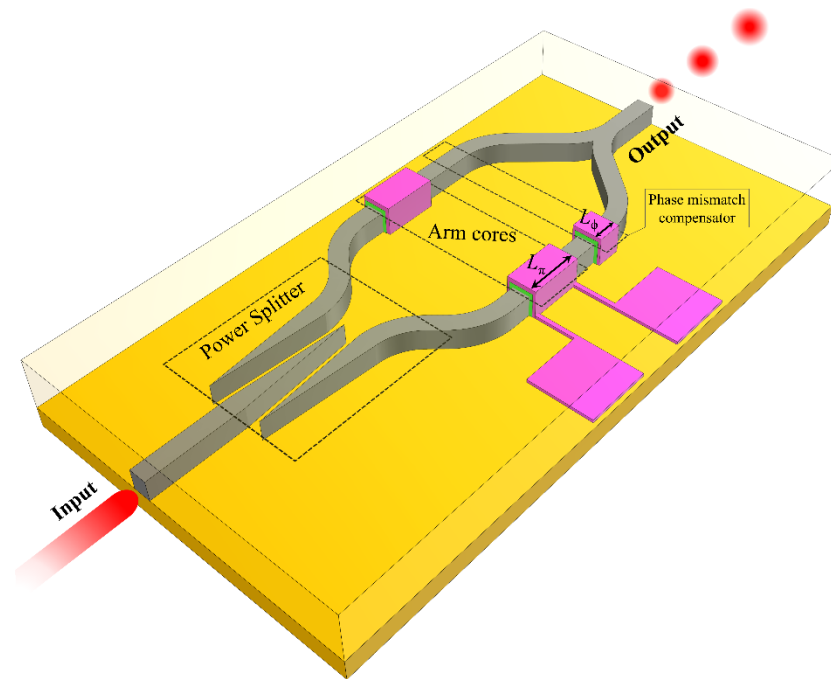

Fig. 5. The designed MZM structure consisting of power splitter at the input, the π-phase shifter arms, and the phase mismatch compensator.

The proposed MZI structure consists of three main parts including a power splitter at the input, π-phase shifter arms, and a phase mismatch compensator illustrated in Fig. 5 that are explained as follows. The arm core basically is used for establishing the π-phase-shift using active and passive arms. A power splitter has been utilized to inject the input light unevenly into the active

and passive arms. This can compensate the loss of the active arm in the crystalline phase by choosing an appropriate power split ratio of the input light. The power splitter comes with a phase difference ($\Delta\phi$) between the two divided lights into the arms. To achieve a high-performance MZM, it is vital to use a phase compensator to reject the mentioned phase difference. The passive and active arms, and the phase compensator are based on the proposed waveguide in section 2.

A three-waveguide tapered directional coupler structure is considered for designing the power splitter. The power ratio of the two power splitter outputs can be determined by spacing of the waveguides. The waveguides in the coupling region are considered to be tapered instead of being uniform. This will increase the mode size of the waveguides, results in an increased modal overlap of the waveguides. In turns, the coupling length would be reduced and lead to a compact device.

The active length of the MZM arms (L_π) can be calculated by the following formula:

$$L_\pi = \frac{\lambda}{2\mathrm{Re}(n_{\mathrm{eff,C}} - n_{\mathrm{eff,A}})} \tag{1}$$

where $n_{\mathrm{eff,C}}$ and $n_{\mathrm{eff,A}}$ are the effective refractive indices for the crystalline and amorphous phases. λ is the operating wavelength which is considered to be 1.55 µm. Here, L_π will be determined to be ~4.3 µm by substituting the calculated values for $n_{\mathrm{eff,C}}$ and $n_{\mathrm{eff,A}}$ in section 2. The loss in the crystalline phase (Γ) is calculated by having the value of L_π as follows:

$$\Gamma = L_\pi \frac{40\pi\mathrm{Im}(n_{\mathrm{eff,C}})}{\lambda\ln(10)} \tag{2}$$

where Γ is calculated to be ~7.2 dB by substituting the corresponding values in (2). The loss in the amorphous phase is low enough to be considered negligible. The divided portion of power light injected into the passive and active arms are denoted as T_1 and T_2, respectively in (3). It is aimed to calculate the ratio of T_1/T_2 to ensure the amplitude of the electric field at the end of arms core will be the same where is calculated as follows by substituting the corresponding values: The coupling loss, CL, for the amorphous phase is very low and it is neglected. The following formula is hold for unity power input in (4):

$$\frac{T_1}{T_2} = 10^{-(\Gamma + T_2\mathrm{CL})/10}. \tag{3}$$

The coupling loss, CL, for the amorphous phase is very low and it is neglected. The following formula is hold for unity power input in (4):

$$T_1 + T_2 = 10^{-\mathrm{SL}/10} \tag{4}$$

where the total insertion loss of the power splitter is denoted as SL. By having T_1 from (4), a formula for calculating T_2 is as follows:

$$T_2 = \frac{10^{-\mathrm{SL}/10}}{1 + T_1/T_2} \tag{5}$$

where T_2 can be calculated by the iteration method by having SL. As mentioned earlier, the power splitter is based on directional couplers with tapered waveguides as similar structures have been reported previously [33–35]. The geometric properties of the power splitter are depicted in Fig. 6(a). The total length of the coupling region is considered to be 5 µm and the distance between the access-waveguide and the power splitter output connected to the active-arm assumed to be 150 nm. Also, the distance between the access-waveguide and the power splitter output connected to the passive-arm is denoted by g. A finite difference time domain (FDTD) simulation

is conducted to find the appropriate value of g by sweeping it from 150 nm to 750 nm to satisfy the uneven division of power between the two arms. At each step of sweep, the portion of the optical power for both arms, T_1/T_2, SL, and $\Delta\phi$ are calculated at the wavelength of 1.55 μm, and the results are depicted in Fig. 6 (a-c).

An approach is deployed for determining g. For this purpose, T_2 must be known for specifying the appropriate amount of g using Fig. 6(a), while (5) implies that T_2 is basically dependent on SL and g itself (Fig. 6(c)). Therefore, the iteration algorithm should be utilized for finding the mentioned parameters as follows. Initially, SL should be considered in a range of -0.8 dB and -0.4 dB, and T_1/T_2 is calculated using (3) and (5). Then, the correspondent g with the calculated T_1/T_2 ratio can be found from Fig. 6(b), and it will be followed with specifying the corresponding SL from Fig. 6(c). Finally, the T_1/T_2 ratio is calculated again having found SL. This process is repeated sufficiently for convergence of g, SL, and T_1/T_2 ratio to their final values, accurately. Here, T_1, T_2, and the ratio of T_1/T_2 using the initial value of SL = -0.5 dB are determined to be 0.135, 0.764, and 0.1767, respectively. Now, g is found to be 340 nm with the corresponding SL = -0.52 dB and $\Delta\phi$ of 29°.
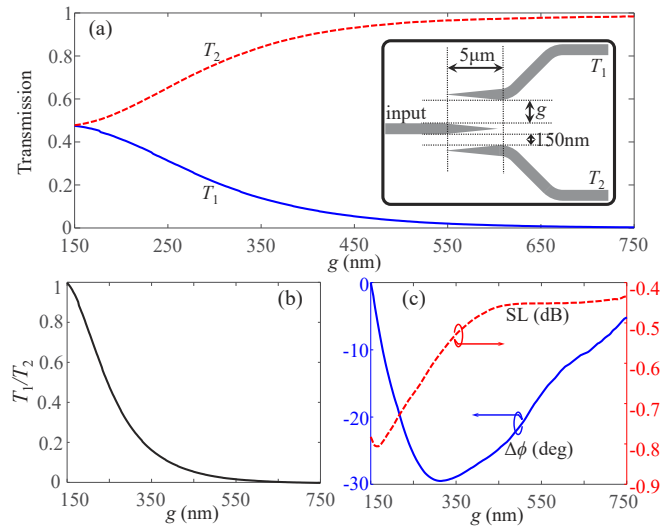

Fig. 6. (a) T_1 and T_2 in the term of g. The inset figure shows the geometric properties of the power splitter. (b) T_1/T_2, (c) SL and $\Delta\phi$ as a function of g at the wavelength of 1.55 μm.

It is not necessary to perform other iterative calculations around $g = 340$ nm due to a tiny difference of the calculated SL (0.52 dB) with the initial value of SL (0.5 dB). The phase shift compensator consists of a Si-waveguide on the MZM passive arm, while the proposed passive waveguide is placed into the active arm. The difference of refractive index between these two waveguides can be exploited to compensate the phase difference introduced by the power splitter. To do so, the length of the phase compensator region (L_ϕ) is calculated to be 600 nm at the wavelength of 1.55 μm by the following formula:

$$L_\phi = \frac{\lambda\Delta\phi}{2\pi\text{Re}(n_{\text{eff,A}} - n_{\text{eff,C}})}. \qquad (6)$$

The design of the proposed MZM structure has been concluded by calculating L_ϕ. Note that the phase mismatch can be compensated by changing the length of one of the two arms or the width of the waveguide locally to modify the effective index. We exploited a passive amorphous layer of GSST due to its compatibility with the device fabrication process without any

further requirements (e.g. lithography process). Also, it can open up a new horizon for extended applications of GSST.

Note that MZMs basically suffer from large footprint since the input/output S-bends are considered to be inseparable components. Elimination of the S-bends potentially leads to a much more compact device. In following, it will be demonstrated that the optical properties of the designed active waveguide combined with very short arms (4.3 μm) of the MZM can be considered for realizing a high-performance bend-less device. The schematic of the bend-less structure can be obtained by eliminating the bends of the proposed MZM (Fig. 5) which is depicted in Fig. 7(a). As it is apparent, instead of conventional Y-junctions, the output power combiner structure is the same as the input power splitter. The difference is the spacing of the arms and the output waveguide (d) that are assumed to be equal. It seems that the reduction in the distance between arms of this structure may cause an unwanted light coupling between them. This could cause a disturbance in the modulation process. To examine this issue, the coupling efficiency between the arms in both ON- and OFF-states are calculated. To do so, the perturbed super-modes established by the vicinity of the arms in the bend-less structure must be calculated in both operating states. The dominant component electric field (E_x) profiles of these super-modes in the OFF-state are shown in Fig. 7(b), c. The percentage of the optical power that couples from one arm to the other can be estimated using $P(L_\pi) = 100\sin^2(\pi L_\pi \Delta n_{eff}/\lambda)$ where Δn_{eff} is the difference of the effective refractive indices of the super-modes. For the OFF-state, $P(L_\pi)$ is calculated to be $\sim 7.5 \times 10^{-6}$% (with $\Delta n_{\text{eff}} = 3 \times 10^{-5}$) confirming a very low coupling between arms can be neglected.
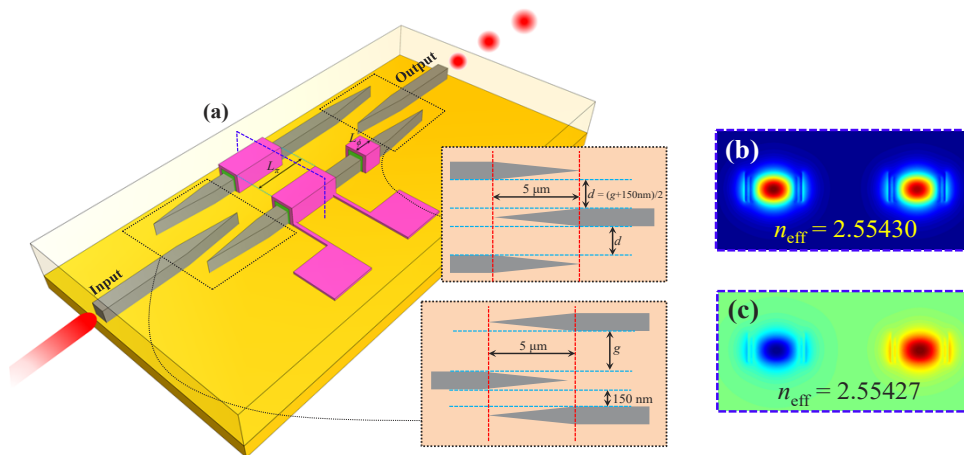

Fig. 7. (a) The proposed bend-less MZM. Dominant component electric field (E_x) profiles for (b) even (c) odd super-modes at OFF-state.

The comparison between the MZM arm length with their coupling length (L_C) (the requisite length for total power transfer from one arm to another) is an additional measure that can be used to determine the coupling efficiency of the bend-less MZM arms. Note that L_C can be estimated by $\lambda/2\Delta n_{eff}$ to be ~26mm. It reveals a negligible optical power coupling between bend-less MZM arms due to the required coupling length of 26 mm to be compared with the arm length of ~4.5 μm. It can be concluded that the coupling issue at the OFF-state between arms of the bend-less MZM is insignificant. On the other hand, at the ON-state, simulations show that none of the arm optical modes are perturbed at the distance of 970 nm between arms due to a very high difference in the effective refractive indices in crystalline and amorphous phases. Thus, no super-mode will be established in the structure based on two arms. It can be interpreted as no

optical coupling between arms of the bend-less MZM at the ON-state. A similar case has been reported earlier [4,25] in designing a high-performance optical switch based on GSST.

This discussion addressed no disturbance in the modulation performance by reducing the distance between arms to ~1 μm (by eliminating the S-bends from the MZM). The optical properties of the designed bend-less MZM within the FDTD simulations including optical power output spectrum and the electric field distribution of the propagating light are represented in Fig. 8 and Fig. 9 respectively. The insertion loss of the bend-less MZM is simulated to be less than 1.7 dB at the entire simulated wavelength range shown in Fig. 8. Note that the unbalance input power of the arms introduces an excessive insertion loss to the device which is a portion of total insertion loss of 1.7 dB. Also, the extinction ratio of the bend-less device is calculated ~50 dB at the wavelength of 1.55 μm and remains greater than 35 dB at 1.5 μm < λ < 1.6 μm. This deigned bend-less MZM with the modified optical characteristics can be introduced as a compact-device for the future applications in silicon photonic platforms.
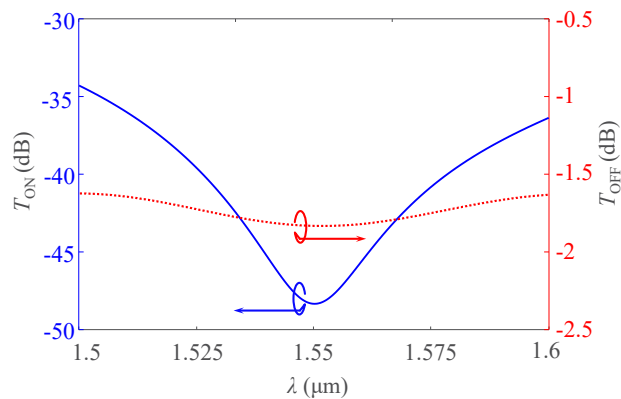

Fig. 8. The output optical power of the bend-less MZM as a function of wavelength in the range of 1.5 μm < λ < 1.6 μm.

3.3. Thermal characterization of the device

Here, the feasibility of phase transition of the GSST layer inserted to the active arm of the proposed bend-less MZM designed in section 3.2. is investigated. The thermal excitation for the phase transition is induced by Joule heating mechanism. The multiphysics electro-thermal simulations using the finite element method (FEM) have been performed based on material parameters including material density, thermal conductivity, and heat capacity. These parameters for those of ITO are reported [36]. It should be noted, the thermal characterization of the GSST material is not found in the literature as the same issue is experienced in [4] and their approach has been used to define the thermal parameters of the GSST layer based on those of GST material [36–38].

A passivation layer of SiO_2 with the thickness of 1000 nm over the simulation regions has been considered to provide much realistic results. Note that ITO is considered as the conductive material of choice for the heater and electrodes. The electrical properties of ITO, particularly the electrical resistivity (ρ) required for the simulations are determined by its free carrier concentration. Specifically, for a given carrier concentration of 1×10^{19} cm^{-3}, ρ is reported as 0.0016 Ω.cm according to experimental measurements [39]. An appropriate voltage pulse with sufficient amplitude and duration is applied to the ITO heater for the amorphous to crystalline phase transition. Our simulations demonstrate that the phase transition from crystalline to amorphous can be obtained with a 10 V pulse. The duration of the pulse required for the
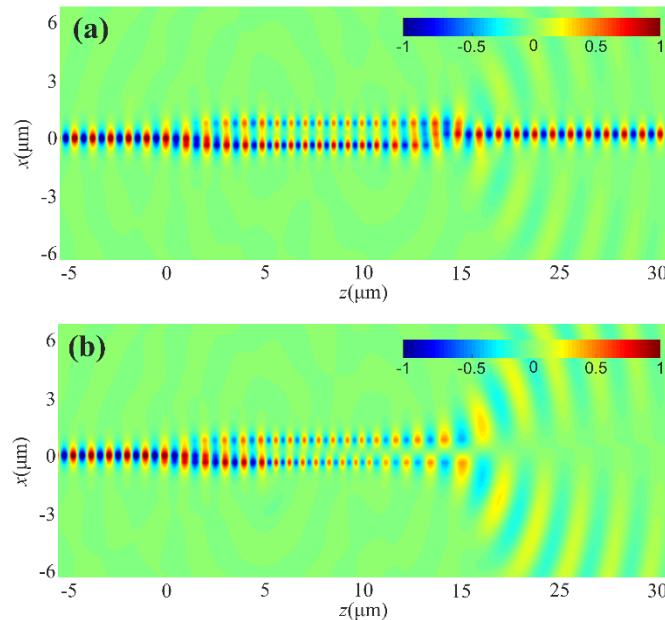
Fig. 9. The dominant optical electric field distribution at the wavelength of 1.55 μm at (a) OFF-state, (b) ON-state.

amorphization process is considered to be the time consumed for raising the temperature of the entire 4.3 μm GSST layer above the melting temperature (~900 K). The simulations are kept processing until the coolest regions become at least 900 K to ensure a complete amorphization. The result determines the pulse width of ~1.8 μs capable of a complete phase transition of the GSST layer from amorphous to the crystalline as is depicted in Fig. 10(a). Also, the temperature distribution profile of the bend-less MZM in the active region at the end of amorphization process is shown in Fig. 10(b). Also, the simulation results have demonstrated that the passive arm is unaffected by the temperature variation of the active arm (Fig. 10(b)). The passive arm will stay in its amorphous phase by the phase transition of the active arm. The total power consumption for the amorphization process is simulated to be 43.6 nJ by considering a voltage pulse width of 1.8 μs.

The phase transition from the amorphous to crystalline is a challenging process in comparison with the amorphization since the GSST layer must be kept at a temperature between the critical temperature (523 K) and the melting temperature point of the GSST material (~900 K) for a specific amount of time (τ_C).

The crystallization can be carried out by maintaining the temperature of the coolest regions at 600 K for a duration of τ_C. To do so, a sequence of voltage pulses is applied to the heater with the amplitude of 10 V, and the appropriate time span. The approach adopted for determining each pulse width of the pulse train is switching "OFF" the heater when the temperature reaches 600 K, and it will be "ON" again when the temperature drops by 10 K. The results are plotted in Fig. 11 that τ_C is reported to be 80 μs [4]. The initial pulse width is calculated to be 2 μs in order to increase the temperature from 300 K to 600 K. It can be resulted from Fig. 11(b) that after initiating the crystallization, the time duration of the following pulses are almost equal to 30 ns to maintain the temperature of the active layer at a crystallization temperature (590 K to 600 K), while the duty cycles are started to be decayed from ~50% to ~10%. Also, the power consumed by the ITO microheater is calculated to be 72.4 nJ.
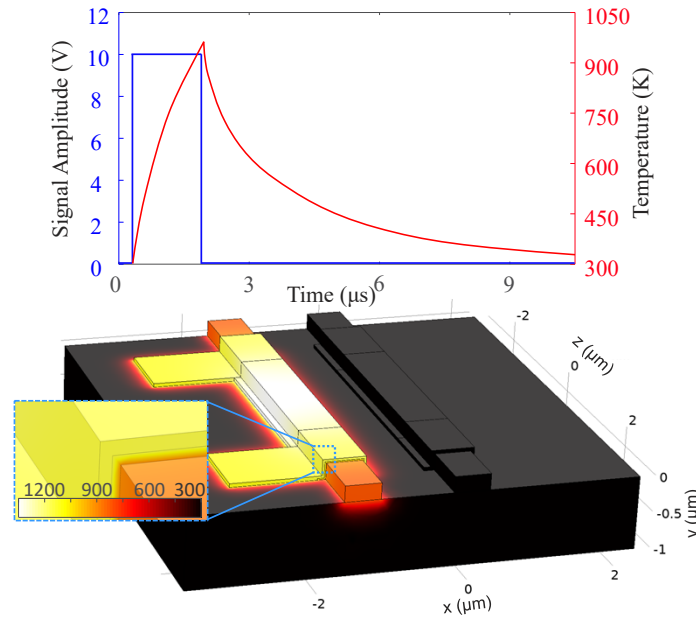
Fig. 10. (a) The excitation signal for the amorphization and the lowest temperature of the GSST layer as a function of time, (b) temperature distribution for the arms of the bend-less MZM.
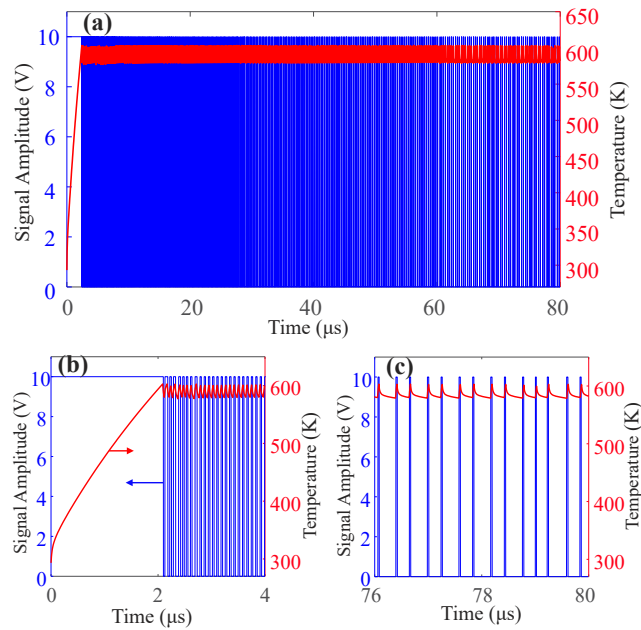

Fig. 11. The required temperature and excitation signal for maintaining the crystallization temperature as a function of time, (a) from 0 to 80 µs, (b) initial 4 µs, (c) final 4 µs (from 76 to 80 µs).

Simulations record an excellent phase transition through a complete amorphization and crystallization by providing an appropriate amount of thermal energy by applying 10 V pulses to the ITO heater to the active arm. This section is closed by indicating the calculated $V_\pi L_\pi$ that is determined to be 43 V.µm.

4.   Conclusions

We have proposed an MZI structure to realize modulation using GSST-based waveguides as the arms. The device is consisting of a power splitter and a phase shifter designed based on FDTD. The properties of the designed active waveguide facilitate designing a much compact bend-less device based on the proposed MZM. The $V_\pi L_\pi$ of 43 V.µm and the insertion loss of ~1.7 dB are calculated for the introduced bend-less MZM with the active length of 4.3 µm. The ITO heater provides the thermal requirements and the electro-thermal characterization including the properties of the actuating voltage signal, power consumption, and phase transition delay of the modulator have been performed using FEM simulations.

Disclosures. The authors declare no conflicts of interest related to this paper.

Data Availability. Data underlying the results presented in this paper are not publicly available at this time but may be obtained from the authors upon reasonable request.

References

1. H. Zhang, L Zhou, B. M. A. Rahman, X. Wu, L. Lu, Y. Xu, J. Xu, J. Song, Z. Hu, L. Xu, and J. Chen, "Ultracompact Si-GST hybrid waveguides for nonvolatile light wave manipulation," IEEE Photonics J. **10**(1), 1–10 (2018).
2. R. Amin, R. Maiti, Y. Gui, C. Suer, M. Miscuglio, E. Heidari, R. Chen, H. Dalir, and V.J. Sorger, "Sub-wavelength GHz-fast broadband ITO Mach–Zehnder modulator on silicon photonics," Optica **7**(4), 333–335 (2020).
3. J. Faneca, T. D. Bucio, F. Y. Gardes, and A. Baldycheva, "O-band N-rich silicon nitride MZI based on GST," Appl. Phys. Lett. **116**(9), 093502 (2020).
4. F. de Leonardis, R. Soref, V. M. N. Passaro, Y. Zhang, and J. Hu, "Broadband electro-optical crossbar switches using low-loss $Ge_2Sb_2Se_4Te_1$ phase change material," J. Lightwave Technol. **37**(13), 3183–3191 (2019).
5. P. Xu, J. Zheng, J. K. Doylend, and A. Majumdar, "Low-loss and broadband non-volatile phase-change directional coupler switches," ACS Photonics **6**(2), 553–557 (2019).
6. M. Liu, X. Yin, E. Ulin-Avila, B. Geng, T. Zentgraf, L. Ju, F. Wang, and X. Zhang, "A graphene-based broadband optical modulator," Nature **474**(7349), 64–67 (2011).
7. H. W. Verleur, A. S. Barker, and C. N. Berglund, "Optical properties of VO_2 between 0.25 and 5 eV," Phys. Rev. **172**(3), 788–798 (1968).
8. B. Janjan, M. Miri, D. Fathi, M. Heidari, and D. Abbott, "Hybrid Si_3N_4/VO_2 modulator thermally triggered by a graphene microheater," IEEE J. Sel. Top. Quantum Electron. **26**(5), 1–6 (2020).
9. M. Sadeghi, B. Janjan, M. Heidari, and D. Abbott, "Mid-infrared hybrid Si/VO_2 modulator electrically driven by graphene electrodes," Opt. Express **28**(7), 9198–9207 (2020).
10. Y. Zhang, J. B. Chou, J. Li, H. Li, Q. Du, A. Yadav, S. Zhou, M. Y. Shalaginov, Z. Fang, H. Zhong, C. Roberts, P. Robinson, B. Bohlin, C. Rios, H. Lin, M. Kang, T. Gu, J. Warner, V. Liberman, K. Richardson, and J. Hu, "Broadband transparent optical phase change materials for high-performance nonvolatile photonics," Nat. Commun. **10**(1), 1–9 (2019).
11. S. Yoo, C. Yoo, E. S. Park, W. Kim, Y. K. Lee, and C. S. Hwang, "Chemical interactions in the atomic layer deposition of Ge-Sb-Se-Te films and their ovonic threshold switching behavior," J. Mater. Chem. C **6**(18), 5025–5032 (2018).
12. C. Rios, Y. Zhang, M. Y. Shalaginov, S. D. Jones, H. Wang, S. An, H. Zhang, M. Kang, K. A. Richardson, C. Roberts, J. B. Chou, V. Liberman, S. A. Vitale, J. Kong, T. Gu, and J. Hu, "Multi-level electro-thermal switching of optical phase-change materials using graphene," Adv. Photonics Res. **2**(1), 2000034 (2021).
13. C. Ríos, Q. Du, Y. Zhang, CC. Popescu, MY. Mikhail, Y. Shalaginov, P. Miller, C. Roberts, M. Kang, KA. Richardson, T. Gu, SA. Vitale, and J. Hu, "Ultra-compact nonvolatile phase shifter based on electrically reprogrammable transparent phase change materials," arXiv preprint arXiv:2105.06010 [cond-mat, physics: physics] (2022).
14. M. Delaney, I. Zeimpekis, D. Lawson, D.W. Hewak, and O.L. Muskens, "A new family of ultralow loss reversible phase-change materials for photonic integrated circuits: Sb_2S_3 and Sb_2Se_3," Adv. Funct. Mater. **30**(36), 2002447 (2020).
15. Z. Fang, J. Zheng, A. Saxena, J. Whitehead, Y. Chen, and A. Majumdar, "Non-volatile reconfigurable integrated photonics enabled by broadband low-loss phase change material," Adv. Opt. Mater. **9**(9), 2002049 (2021).
16. K. Kato, M. Kuwahara, H. Kawashima, T. Tsuruoka, and H. Tsuda, "Current-driven phase-change optical gate switch using indium tin-oxide heater," Appl. Phys. Express **10**(7), 072201 (2017).
17. V. Weidenhof, I. Friedrich, S. Ziegler, and M. Wuttig, "Laser induced crystallization of amorphous $Ge_2Sb_2Te_5$ films," J. Appl. Phys. **89**(6), 3168–3176 (2001).

18. S. M. Pouyan, M. Miri, and M. H. Sheikhi, "Design of a vanadium dioxide-based dual-polarization optical PAM4 modulator," J. Opt. Soc. Am. B **35**(12), 3094–3103 (2018).

19. H. M. K. Wong, Z. Yan, K. A. Hallman, R. E. Marvel, R. P. Prasankumar, R. F. Haglund Jr., and A. S. Helmy, "Broadband, integrated, micron-Scale, all-optical Si_3N_4/VO_2 modulators with pJ switching energy: supporting information," ACS Photonics **6**(11), 2734–2740 (2019).

20. Z. Yu, J. Zheng, P. Xu, W. Zhang, and Y. Wu, "Ultracompact electro-optical modulator-based $Ge_2Sb_2Te_5$ on silicon," IEEE Photonics Technol. Lett. **30**(3), 250–253 (2018).

21. M. Miscuglio, J. Meng, A. Mehrabian, V. J. Sorger, O. Yesiliurt, L. J. Prokopeva, A. V. Kildishev, Y. Zhang, and J. Hu, "Artificial synapse with mnemonic functionality using GSST-based photonic integrated memory," Appl. Comput. Electromagn. Soc. J. **35**(11), 1447–1449 (2021).

22. M. Y. Shalaginov, S. An, Y. Zhang, and F. Yang, "Reconfigurable all-dielectric metasurfaces based on optical phase change materials: design approaches," in *International Applied Computational Electromagnetics Society Symposium (ACES)*, 1–2 (2020).

23. S. M. Pouyan, M. Miri, and M. H. Sheikhi, "Design and numerical analysis of a high-performance optical modulator based on Si-VO_2 bragg grating waveguide," Appl. Opt. **60**(5), 1083–1091 (2021).

24. K. J. Miller, R. F. Haglund, and S. M. Weiss, "Optical phase change materials in integrated silicon photonic devices: review," Opt. Mater. Express **8**(8), 2415–2429 (2018).

25. Q. Zhang, Y. Zhang, J. Li, R. Soref, T. Gu, and J. Hu, "Broadband nonvolatile photonic switching based on optical phase change materials: beyond the classical figure-of-merit," Opt. Lett. **43**(1), 94–97 (2018).

26. J. Song, S. Ghosh, H. Zhang, L. Zhou, and B. M. A. Rahman, "Design, optimization, and performance evaluation of GSST clad low-loss non-volatile switches," Appl. Opt. **58**(31), 8687–8694 (2019).

27. N. Youngblood, C. Talagrand, B. Porter, C. G. Galante, S. Kneepkens, S. G. Sarwat, D. Yarmolich, R.S. Bonilla, P. Hosseini, R. Taylor, and H. Bhaskaran, "Broadly-tunable smart glazing using an ultra-thin phase-change material," arXiv preprint arXiv:1911.02990 (2019).

28. H. Zhang, L. Zhou, L. Lu, J. Xu, N. Wang, H. Hu, B. A. Rahman, Z. Zhou, and J. Chen, "Miniature multilevel optical memristive switch using phase change material," ACS Photonics **6**(9), 2205–2212 (2019).

29. J. Zheng, S. Zhu, P. Xu, S. Dunham, and A. Majumdar, "Modeling electrical switching of nonvolatile phase-change integrated nanophotonic structures with graphene heaters," ACS Appl. Mater. Interfaces **12**(19), 21827–21836 (2020).

30. J. Zheng, Z. Fang, C. Wu, S. Zhu, P. Xu, J. K. Doylend, S. Deshmukh, E. Pop, S. Dunham, M. Li, and A. Majumdar, "Nonvolatile electrically reconfigurable integrated photonic switch enabled by a silicon PIN diode heater," Adv. Mater. **32**(31), 2001218 (2020).

31. N. Farmakidis, N. Youngblood, J. S. Lee, J. Feldmann, A. Lodi, X. Li, S. Aggarwal, W. Zhou, L. Bogani, W. H. Pernice, and C. D. Wright, "Electronically reconfigurable photonic switches incorporating plasmonic structures and phase change materials," Adv. Sci. 2200383 (2022).

32. P. O. Oviroh, R. Akbarzadeh, D. Pan, R. A. M. Coetzee, and T. C. Jen, "New development of atomic layer deposition: processes, methods and applications," Sci. and Technol. Adv. Mater. **20**(1), 465–496 (2019).

33. V. H. Nguyen, I. K. Kim, and T. J. Seok, "Low-loss and broadband silicon photonic 3-db power splitter with enhanced coupling of shallow-etched rib waveguides," Appl. Sci. **10**(13), 4507 (2020).

34. H. Kim and H. Shin, "Tailorable and broadband on-chip optical power splitter," Appl. Sci. **9**(20), 4239 (2019).

35. Y. Wang, S. Gao, K. Wang, and E. Skafidas, "Ultra-broadband and low-loss 3 dB optical power splitter based on adiabatic tapered silicon waveguides," Opt. Lett. **41**(9), 2053–2056 (2016).

36. C. Rios, M. Stegmaier, Z. Cheng, N. Youngblood, C. D. Wright, W. H. P. Pernice, and H. Bhaskaran, "Controlled switching of phase-change materials by evanescent-field coupling in integrated photonics," Opt. Mater. Express **8**(9), 2455–2470 (2018).

37. E. Bozorg-Grayeli, J. P. Reifenberg, K. W. Chang, M. Panzer, and K. E. Goodson, "Thermal conductivity and boundary resistance measurements of GeSbTe and electrode materials using nanosecond thermoreflectance," in *12th IEEE Intersociety Conference on Thermal and Thermomechanical Phenomena in Electronic Systems* (2010), 1–7.

38. P. K. Khulbe, X. Xun, and M. Mansuripur, "Crystallization and amorphization studies of a $Ge_2Sb_{2.3}Te_5$ thin-film sample under pulsed laser irradiation," Appl. Opt. **39**(14), 2359–2366 (2000).

39. Y. Gui, M. Miscuglio, Z. Ma, M. H. Tahersima, S. Sun, R. Amin, H. Dalir, and V. J. Sorger, "Towards integrated metatronics: a holistic approach on precise optical and electrical properties of indium tin oxide," Sci. Rep. **9**(1), 1–10 (2019).